


## Quasibound states in continuum-induced double strong coupling in perovskite and WS<sub>2</sub> monolayers

Ibrahim A. M. Al-Ani <sup>1</sup>, Khalil As'Ham <sup>1</sup>, Mohammed Alaloul,<sup>1</sup> Lei Xu <sup>2</sup>,  
Haroldo T. Hattori,<sup>1</sup> Lujun Huang <sup>1,\*</sup> and Andrey E. Miroshnichenko<sup>1,†</sup>

<sup>1</sup>*School of Engineering and Information Technology, University of New South Wales at Canberra, Northcott Drive, Canberra, Australian Capital Territory 2610, Australia*

<sup>2</sup>*Advanced Optics and Photonics Laboratory, Department of Engineering, School of Science and Technology, Nottingham Trent University, Nottingham NG11 8NS, United Kingdom*



(Received 1 September 2022; revised 29 June 2023; accepted 6 July 2023; published 26 July 2023)

In recent years, the formation of exciton-polaritons in semiconductor materials has attracted major interest because of their exotic optical properties, allowing the study of many interesting physical phenomena, such as superfluids and Bose-Einstein condensation. Here, we demonstrate a double strong coupling regime in a perovskite and tungsten disulfide (WS<sub>2</sub>) monolayer using single and dual quasibound states in the continuum (QBIC). Except for supporting exciton resonance, bi(phenethylammonium)tetraiodoplumbate perovskite thin film is patterned as a grating to act as a single symmetry-protected bound state in the continuum (BIC) or dual BICs by harnessing its high index. A WS<sub>2</sub> monolayer is sandwiched inside the perovskite nanowire so that a single BIC can be strongly coupled to both exciton resonances of perovskite and WS<sub>2</sub> monolayers with a Rabi splitting of 380 and 42.2 meV. We found that the  $Q$  factor and thickness of perovskite film play a central role in governing the coupling strength. In addition, we demonstrate that double strong coupling can be satisfied by using dual QBICs, where each QBIC is individually coupled to the exciton of either a perovskite or a WS<sub>2</sub> monolayer. The design approach achieves a Rabi splitting as high as 353.6 and 31.80 meV in the perovskite and the WS<sub>2</sub> monolayer, respectively. This is a demonstration of a double strong coupling regime using a single structure based on perovskite and WS<sub>2</sub> monolayers. The realization of double strong coupling paves the way for the emergence of polaritonic devices with advanced functionalities, such as dual wavelength polariton nanolasers.

DOI: [10.1103/PhysRevB.108.045420](https://doi.org/10.1103/PhysRevB.108.045420)

### I. INTRODUCTION

The strong coupling between excitons and a photonic microcavity has been extensively studied in recent years [1–7]. When the excitons of semiconductor materials are strongly coupled to a photonic cavity, a new mixed state called an exciton-polariton is formed. Typically, the strong coupling is featured by an avoided crossing in the dispersion relationship. A system falls within the strong coupling regime and forms exciton-polaritons when the energy exchange rates between light and matter exceed their decoherence rates. The newly developed mixed states preserve their quantum states and combine the advantages of both photons and excitons, leading to the emergence of many applications and technologies such as ultralow threshold polariton lasing, ultrafast all-optical switching, and quantum information processing and transfer technologies [8]. Motivated by its unique properties and great potential in nanophotonic applications, many efforts have been devoted to the realization of the strong coupling regime within various semiconductor materials, including gallium arsenide, zinc oxide, organic materials, quantum dots, perovskites, and transition metal dichalcogenide (TMDC)

monolayers [7,9–12]. However, authors of most of the previous studies reported the observation of strong coupling in a single semiconductor material. It might be appealing to achieve strong coupling simultaneously in two different semiconductors at room temperature, as it may expand the functionalities of the exciton-polariton system.

Several groups have reported double strong coupling regimes in semiconductors in the last two decades. Agronovich *et al.* [13] theoretically demonstrated strong coupling in a cavity composed of organic material and an inorganic semiconductor, resulting in the formation of new hybrid states, including the lower polariton (LP), middle polariton, and upper polariton (UP) branches. Later, authors of several experimental studies reported the realization of double strong coupling in several semiconductor materials such as GaAs quantum wells [14], molecular dyes [15,16], dye zinc tetraphenyl-porphyrin (ZnTPP) and perovskites [17], and ZnO-perovskite [18] sandwiched in optical microcavities made from two mirrors [19,20]. However, these microcavities suffer from several drawbacks, such as complex fabrication processes, bulky integration, and inflexible mode engineering. Following that, plasmonic nanostructures were proposed in several reports to demonstrate double strong coupling due to their ability to provide small mode volume [21–27]. For example, the double strong coupling was demonstrated experimentally in a J-aggregate-doped polyvinyl alcohol (PVA)

\*ljhuang@mail.sitp.ac.cn

†andrey.miroshnichenko@unsw.edu.au

layer sandwiched between a silver grating and a thick silver film [21]. Surface plasmon polaritons (SPPs) with strongly dispersive photonic features and the Fabry-Perot (FP) mode with nearly nondispersive photonic features are both supported by this nanostructure design. Three hybrid polariton bands emerged by tuning the energies of FP and SPPs around the exciton via tuning the thickness of the doped PVA layer and the incident angle, confirming the entry of the system into the double strong regime. However, the lossy nature of plasmonic nanostructures may limit the application of such a system. It is also worth mentioning that most of the previous studies on double strong coupling were carried out at low temperatures. It is highly desirable to realize double strong coupling at room temperature, which is essential for developing practical applications.

Furthermore, it should be noted that most early research used either two exciton modes and one photonic mode or two photonic modes and one exciton mode to achieve the double strong coupling regime. However, the double strong coupling regime between two exciton resonances and two photonic modes is yet to be proposed. In real applications, it is desirable to achieve simultaneously strong coupling in two different materials in one platform, other than building two separate designs. With this approach, we can realize simultaneous strong coupling in two materials based on the same device, which is advantageous over building two separate designs. Furthermore, it has been shown in several investigations that condensation, which is required to produce a polariton laser, occurs in the LP mode in the strong coupling regime [28–30]. Considering this, demonstrating double strong coupling employing two excitons and two photonic modes in a single device will give rise to two LPs, which might be a more practical method of producing dual-wavelength polariton lasers.

Lead halide perovskites and TMDC monolayers are emerging materials with many interesting physical and chemical properties. Both materials have a direct band gap, thus enabling high luminescence quantum yield, making them attractive candidates for next-generation photonic devices. On the other hand, they have large exciton binding energy at room temperature, rendering them ideal platforms for realizing exciton-polaritons at room temperature [27,31–48]. As both perovskite and TMDC monolayer exciton resonances are within the visible wavelength range, it is possible to develop strong coupling simultaneously in both perovskites and TMDC monolayers if they are integrated into a photonic cavity whose resonant wavelength passes through their exciton resonance wavelengths. In addition, lead halide perovskite has a relatively high refractive index 2.0–2.4 around the exciton resonance. It has been well established that high-index semiconductors support multipolar electric and magnetic Mie resonance [49]. In recent years, an interesting concept called bound states in the continuum (BICs) has triggered intensive interest in the photonic communities because it enables strong field confinement in nanostructures [50–54]. A BIC corresponds to a trapping mode despite being located within the continuum. It is a leaky mode with zero radiative decay rate or an infinitely large  $Q$  factor. In real applications, BICs must be transitioned into quasi-BICs (QBICs) to be accessed by external excitation like a plane wave or vector beam. Thanks to their large field enhancement, QBICs have been widely

used to enhance light-matter interaction, such as lasing, enhanced nonlinear harmonic generation, and strong coupling [51,55–61].

In this paper, we demonstrate a room-temperature double strong coupling between excitons and high- $Q$  mode based on QBICs in a hybrid perovskite- $\text{WS}_2$  monolayer system. By taking advantage of the high refractive index of a perovskite, perovskite thin film is patterned as a grating structure to support either a single symmetry-protected, broken, or double BICs. By placing a  $\text{WS}_2$  monolayer inside the perovskite and grating, the double strong coupling is achieved between a single QBIC and exciton resonances of the perovskite and  $\text{WS}_2$  monolayers. Further study indicates that coupling strengths become saturated at a certain  $Q$  factor of the QBIC mode, while they show the opposite trend with increasing thickness. Also, the double strong coupling is realized with dual QBIC modes, while each QBIC is separately coupled to the exciton of different materials. Our design paves the way for the emergence of polaritonic devices such as dual-wavelength polariton nanolasers.

## II. RESULTS AND DISCUSSION

### A. Geometry structure and numerical model

We start by considering a one-dimensional bi(phenethylammonium)tetraiodoplumbate (PEPI) perovskite grating on top of a glass substrate. The refractive index of glass is 1.46, while the permittivity of PEPI perovskite is expressed as follows:

$$\varepsilon(E) = \varepsilon_B + \frac{f}{E_{\text{exciton}}^2 - E^2 - i\Gamma E}, \quad (1)$$

where  $\varepsilon_B$  is the background dielectric constant,  $f$  is the oscillator strength,  $E_{\text{exciton}}$  is the exciton energy, and  $\Gamma$  is the width of the exciton, which are set to  $\varepsilon_B = 5.76$ ,  $f = 0.85 \text{ eV}^2$ ,  $E_{\text{exciton}} = 2.394 \text{ eV}$ , and  $\Gamma = 0.03 \text{ eV}$ , respectively [62,63].

According to previous studies [41,61,64,65], a dielectric grating supports a series of leaky modes characterized by complex eigenfrequencies. To calculate the complex eigenfrequencies of these leaky modes, we used the finite element method provided by the COMSOL software. First, we constructed a model of the one-dimensional PEPI perovskite grating on top of the glass substrate, considering the refractive index of both materials. The refractive index of the perovskite is set as  $n = 2.4$  for the sake of simplicity. Then we defined the polarization of the electromagnetic waves as transverse electric (TE) with the electric field parallel to the grating axis. By solving Maxwell's equations for the model, we can obtain complex frequencies of leaky modes, which are expressed as  $\omega = \omega_0 - i\gamma$ , where  $\omega_0$  and  $\gamma$  represent the resonant frequency and radiative decay rates of leaky modes, respectively. Finally, by analyzing the electric field distribution and corresponding resonant frequencies, we found that some of these leaky modes, such as  $\text{TE}_{21}$  and  $\text{TE}_{22}$ , are symmetry-protected BICs.

The reflection and transmission properties of the proposed nanostructure were determined using the rigorous coupled wave analysis method, which is a well-known numerical technique of investigating the behavior of electromagnetic waves in periodic structures. The nanostructure, consisting of air,

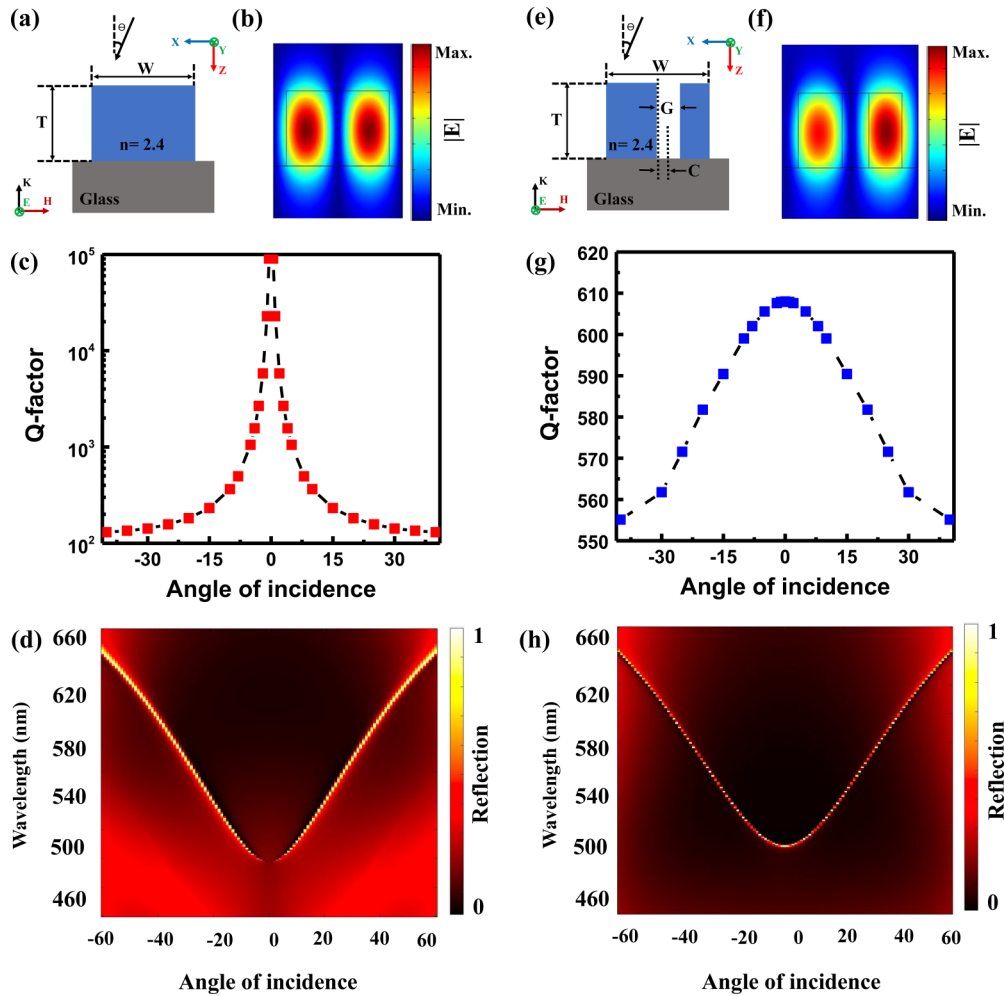


FIG. 1. Design of single quasibound state in the continuum (QBIC) resonance. (a) Two-dimensional (2D) schematic illustration of a unit cell of the nanostructure that supports symmetry-protected QBICs. (b) Electric field distribution of the symmetry-protected QBIC based on the  $TE_{21}$  mode. (c)  $Q$  factor as a function of the angle of incidence of the symmetry-protected QBIC mode showing ideal bound state in the continuum (BIC) with an infinitely large  $Q$  factor at normal incidence. (d) The mapping data of the reflection spectrum of the nanostructure supports the symmetry-protected QBIC resonance as a function of the angle of incidence. Here, the reflection spectra were obtained by considering both perovskite and glass as lossless materials with refractive indices set to 2.4 and 1.46, respectively. (e) 2D schematic illustration of a unit cell of the nanostructure that supports symmetry-broken QBICs with off-centered silt. (f) Electric field distribution of the symmetry-broken QBIC based on the  $TE_{21}$  mode. (g)  $Q$  factor as a function of the angle of incidence of the symmetry-broken QBIC mode showing a finite  $Q$  factor at normal incidence. (h) The mapping data of the reflection spectrum of the nanostructure support the symmetry-broken QBIC resonance as a function of the angle of incidence. Here, the reflection spectra were obtained by considering both perovskite and glass as lossless materials with refractive indices set to 2.4 and 1.46, respectively.

glass, and perovskite grating layers, was analyzed by solving Maxwell’s equations for each layer and then combining the solutions using a matrix formalism to obtain an overall solution for the entire structure. By comparing the amplitude of the reflected and transmitted waves to that of the incident wave, the reflection and transmission coefficients could be calculated accurately and rigorously. Finally, the absorption of the nanostructure can be calculated by subtracting the reflection and transmission coefficients from unity.

**B. Single BIC property of lossless perovskite gratings**

A two-dimensional (2D) schematic representation of the proposed nanostructure unit cell based on PEPI nanowires (NWs) is shown in Fig. 1(a). Figure 1(b) shows the electric

field distribution of the  $TE_{21}$  mode of the symmetry-protected BIC. From the perspective of practical applications, BICs should be transitioned to QBICs with finite  $Q$  factors to be excited with external sources like a plane wave or vector beam. Introducing oblique incidence is one way to convert an ideal BIC to a QBIC. The period ( $P$ ), thickness ( $T$ ) and width ( $W$ ) of the NWs are set as 240, 140, and 190 nm, respectively. The  $Q$  factor as a function of the incident angle is presented in Fig. 1(c). The  $Q$  factor of the BIC mode is calculated as  $Q = \omega_0/2\gamma$ . As shown in the figure, the  $Q$  factor approaches infinity at normal incidence. As the angle of incidence deviates from normal, the  $Q$  factor gradually reduces to a finite  $Q$  factor, and thus a BIC is evolved into a QBIC mode. Such an evolution is verified by the reflection spectra as functions of incident angle and incident wavelength, as

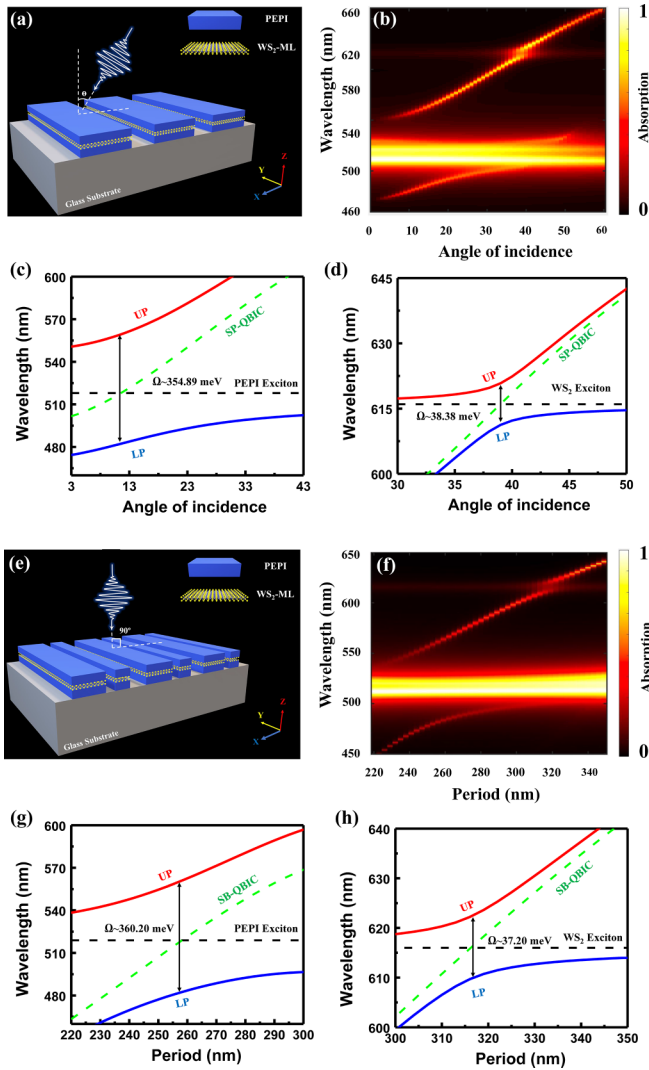


FIG. 2. Double strong coupling realization in a PEPI and WS<sub>2</sub> monolayer based on single bound-state-in-the-continuum (BIC) mode. (a) Three-dimensional (3D) schematic drawing of the symmetry-protected nanostructure where the WS<sub>2</sub> monolayer is sandwiched between the two parts of the PEPI nanowires (NWs). (b) Mapping data of the absorption spectrum as a function of the angle of incidence on the symmetry-protected nanostructure. Here, the absorption spectra were obtained by considering perovskite as a lossy material with a permittivity calculated using Eq. (1) and glass as a lossless material with refractive index set to 1.46. (c) The dispersion of the upper polariton (UP) and lower polariton (LP) branches (solid red and blue lines, respectively) as a function of the angle of incidence of the strong coupling between the symmetry-protected quasibound state in the continuum (QBIC; dashed green line) and the PEPI exciton (dashed black line). (d) The dispersion of the UP and LP branches (solid red and blue lines, respectively) as a function of the angle of incidence of the strong coupling between the symmetry-protected QBIC (dashed green line) and the WS<sub>2</sub> monolayer exciton (dashed black line). (e) 3D schematic drawing of the symmetry-broken nanostructure with an off-centered slit. Here, the WS<sub>2</sub> monolayer is sandwiched between the two parts of the PEPI NWs. (f) Mapping data of the absorption spectrum as a function of the period of the structure of the symmetry-broken nanostructure. Here, the absorption spectra were obtained by considering perovskite as a lossy material with a permittivity calculated using Eq. (1) and

shown in Fig. 1(d). The resonant linewidth indeed disappears at normal incidence, confirming the presence of the ideal BIC mode with an infinite  $Q$  factor. Since we want to realize double strong coupling in both perovskite and WS<sub>2</sub> monolayers, the structure parameters are finetuned to ensure that the QBIC mode intersects with the exciton resonances of the perovskite and WS<sub>2</sub> monolayers when the incident angle varies.

Another way to excite the QBIC mode is to break the symmetry of the unit cell. Here, we introduce an off-centered slit in the perovskite NW to convert the ideal BIC into a QBIC, as shown in the 2D schematic drawing in Fig. 1(e). The period ( $P$ ), thickness ( $T$ ), width ( $W$ ), gap width ( $G$ ), and the distance between the center of the gap and the center of the unit cell ( $C$ ) of the NWs are set to be 255, 140, 195, 50, and 10 nm, respectively. Figure 1(f) shows the electric field distribution of the symmetry-broken QBIC based on the TE<sub>21</sub> mode. Also, we calculated the  $Q$  factor of the symmetry-broken-induced QBIC while sweeping the angle of incidence from  $-60^\circ$  to  $60^\circ$ , as shown in Fig. 1(g). However, in contrast to the symmetry-protected QBIC, the  $Q$  factor of the symmetry-broken QBIC is finite even at normal incidence. This is also confirmed by the reflection spectrum mapping, where the resonant peak is always observed at all studied angles, as shown in Fig. 1(h).

### C. Optical response and physics of strong coupling system

After confirming a QBIC could cross both exciton resonances of perovskite and WS<sub>2</sub> monolayers, we move to demonstrate double strong coupling in both materials. Here, we use the permittivity of PEPI perovskite in Eq. (1), while the permittivity of monolayer WS<sub>2</sub> is taken from Refs. [48,66,67] (see Fig. S1 in the Supplemental Material [68]). To maximize coupling strength between a WS<sub>2</sub> monolayer and a photonic cavity, we sandwiched the WS<sub>2</sub> monolayer at the maximum electric field, which is slightly below the center of the perovskite NWs due to the presence of substrate, as schematically shown in Fig. 2(a). Here,  $P$ ,  $T$ , and  $W$  are set to be 240, 140, and 190 nm, respectively. Figure 2(b) shows the mapping data of the absorption spectrum as a function of the incident angle while the QBIC is strongly coupled to both excitons of the PEPI perovskite and the WS<sub>2</sub> monolayer. Two anticrossings are clearly observed, indicating double strong coupling in both materials as the incident angle is swept from  $0^\circ$  to  $60^\circ$ . It is observed that the anticrossing of the PEPI perovskite happens at  $\sim 11^\circ$ , whereas for the WS<sub>2</sub> monolayer, it occurs at  $\sim 38^\circ$ .

The coupling strength of the system is quantified by calculating the Rabi splitting using a double oscillator model that

glass as a lossless material with refractive index set to 1.46. (g) The dispersion of the UP and LP branches (solid red and blue lines, respectively) as a function of the period of the structure, for the strong coupling between the symmetry-broken QBIC (dashed green line) and the PEPI exciton (dashed black line). (h) The dispersion of the UP and LP branches (solid red and blue lines, respectively) as a function of the period of the structure for the strong coupling between the symmetry-broken QBIC (dashed green line) and the WS<sub>2</sub> monolayer exciton (dashed black line).

accounts for the PEPI perovskite and TMDC excitons:

$$\begin{pmatrix} E_{\text{QBIC}} - i\gamma_{\text{QBIC}} & g \\ g & E_{\text{exciton}} - i\gamma_{\text{exciton}} \end{pmatrix} \begin{pmatrix} \alpha \\ \beta \end{pmatrix} = E_{\pm} \begin{pmatrix} \alpha \\ \beta \end{pmatrix}, \quad (2)$$

where  $E_{\text{QBIC}}$  and  $2\gamma_{\text{QBIC}}$  are referred to as the uncoupled QBIC mode resonance energy and full width of half maximum (FWHM), respectively. Here,  $E_{\text{exciton}}$  and  $2\gamma_{\text{exciton}}$  are the energy and FWHM of either the TMDC monolayer or PEPI excitons, respectively. Also,  $E_+$  and  $E_-$  are the energies of the UPs and LPs, which can be calculated as

$$E_{\pm} = \frac{(E_{\text{QBIC}} + E_{\text{exciton}}) - i(\gamma_{\text{QBIC}} + \gamma_{\text{exciton}})}{2} \pm \sqrt{g^2 - \frac{[E_{\text{QBIC}} - E_{\text{exciton}} + i(\gamma_{\text{QBIC}} - \gamma_{\text{exciton}})]^2}{4}}. \quad (3)$$

The Rabi splitting value ( $\Omega$ ) is extracted from the reflection mapping data at the anticrossing point where  $E_{\text{QBIC}} - E_{\text{exciton}} = 0$ . The coupling strength ( $g$ ) of the coupled system is then calculated as

$$g = \frac{\sqrt{\Omega^2 + (\gamma_{\text{QBIC}} - \gamma_{\text{exciton}})^2}}{2}. \quad (4)$$

After obtaining the coupling strength, the dispersion relations of the UPs and LPs are obtained. Figure 2(c) shows the UP and LP branches of the strong coupling regime between the symmetry-protected QBIC and the PEPI exciton. The exciton resonance and QBIC are also plotted in dashed lines as references. The fitted data of the UPs and LPs match well with the mapping data of the absorption spectrum in Fig. 2(b). The anticrossing behavior happens at  $\sim 11^\circ$ , yielding a Rabi splitting and coupling strength of  $\sim 354.89$  meV and  $\sim 177.48$  meV, respectively. Similarly, we calculate the UP and LP energies of the strong coupling between the QBIC and the exciton of the  $\text{WS}_2$  monolayer. The fitted data are presented in Fig. 2(d). The exciton resonance and QBIC are also plotted in dashed lines as references showing anticrossing behavior happens at  $\sim 38^\circ$ . The Rabi splitting and coupling strength are calculated to be  $\sim 38.38$  meV and  $\sim 19.48$  meV, respectively.

We also retrieve the eigenvectors  $\alpha$  and  $\beta$ , representing the weighting coefficients of the exciton and QBICs in the two polariton bands to better understand the coupling process. The exciton and photon fractions in the UP and LP are given by the squared amplitude of the coefficients of the eigenvectors ( $|\alpha|^2$  and  $|\beta|^2$ ). The calculated fractions for the UP and LP bands of the PEPI and  $\text{WS}_2$  monolayer are shown in Fig. 3. One can also notice that the condition  $|\alpha|^2 + |\beta|^2 = 1$  is satisfied in all cases. The formation of the strongly coupled exciton-polariton is further confirmed by checking the following conditions:

$$g > \frac{|\gamma_{\text{QBIC}} - \gamma_{\text{exciton}}|}{2}, \text{ and } g > \frac{\sqrt{(\gamma_{\text{QBIC}})^2 + (\gamma_{\text{exciton}})^2}}{4}. \quad (5)$$

Following a similar strategy, we also demonstrate the strong coupling of both PEPI perovskite and  $\text{WS}_2$  monolayer excitons for the case of a symmetry-broken QBIC at a

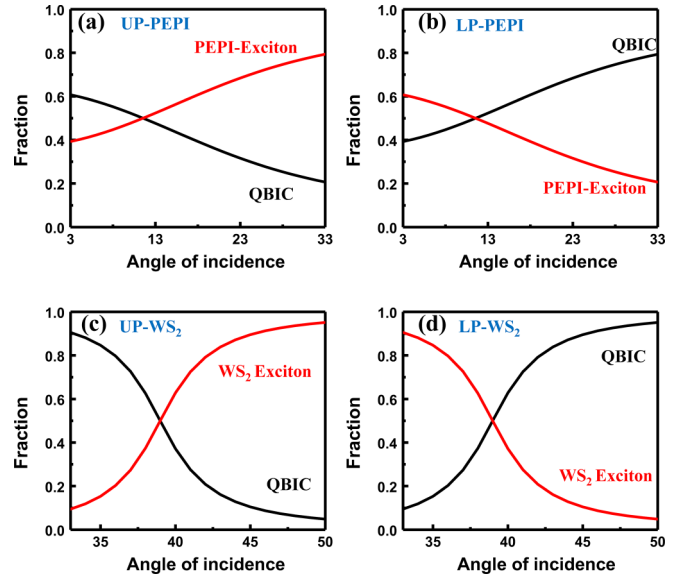


FIG. 3. Fraction of the polariton branches of the double strong coupling based on symmetry-protected quasibound state in the continuum (QBIC). (a) Fractions of the upper polariton (UP) branch of the strong coupling between symmetry-protected QBIC in solid black and PEPI-exciton in solid red as a function of the angle of incidence. (b) Fractions of the lower polariton (LP) branch of the strong coupling between symmetry-protected QBIC in solid black and PEPI-exciton in solid red as a function of the angle of incidence. (c) Fractions of the UP branch of the strong coupling between symmetry-protected QBIC in solid black and  $\text{WS}_2$  monolayer exciton in solid red as a function of the angle of incidence. (d) Fractions of the LP branch of the strong coupling between symmetry-protected QBIC in solid black and  $\text{WS}_2$  monolayer exciton in solid red as a function of the angle of incidence.

normal incidence. Figure 2(e) shows the schematic drawing of the symmetry-broken-induced QBIC structures with the  $\text{WS}_2$  monolayer placed slightly below the center of the PEPI perovskite NW. Here, we set  $T$ ,  $W$ ,  $G$ , and  $C$  to be 140, 210, 50, and 10 nm, respectively. The mapping data of the absorption spectrum as a function of the period of the structure at a normal incidence is shown in Fig. 2(f). The period of the structure is swept from 220 to 300 nm. The anticrossing behavior of the symmetry-broken QBIC and PEPI exciton occurs at a period of  $\sim 256$  nm.

In comparison, the anticrossing of the symmetry-broken QBIC and  $\text{WS}_2$  exciton occurs at a period of  $\sim 316$  nm. We also fitted the UP and LP branches of strong coupling between the symmetry-broken-induced QBIC and PEPI perovskite and the  $\text{WS}_2$  monolayer excitons using the double oscillator model presented in Figs. 2(g) and 2(h), respectively. The Rabi splitting and the PEPI perovskite exciton-polariton coupling strength are calculated to be  $\sim 360.20$  meV and  $\sim 180.10$  meV, respectively. The Rabi splitting and the coupling strength of the  $\text{WS}_2$  monolayer exciton-polariton are calculated to be  $\sim 37.20$  meV and  $\sim 18.60$  meV, respectively. We also retrieve the eigenvectors  $\alpha$  and  $\beta$  of the strong coupling between the symmetry-broken-induced QBIC and both semiconductor materials. The fractions of the UP and LP of both strong couplings are presented in Fig. S2 in the Supplemental Material [68].

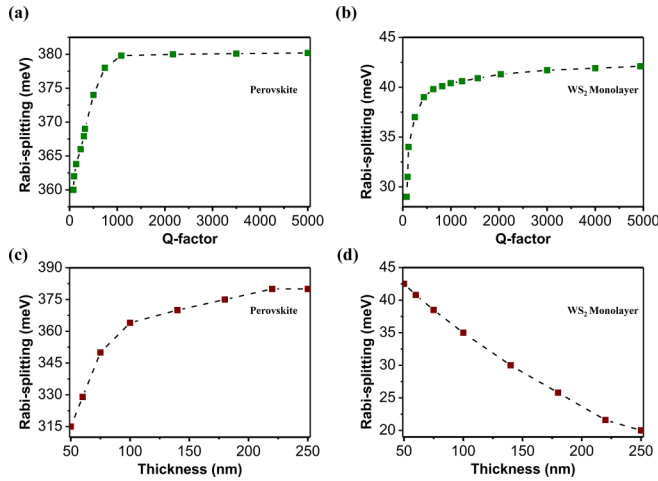


FIG. 4. Rabi splitting dependence of  $Q$  factor and the thickness of the nanostructure. (a) Rabi splitting of the strong coupling between the perovskite and the symmetry-broken quasibound state in the continuum (QBIC) as a function of the  $Q$  factor. Here, sweeping  $C$  swept the  $Q$  factor, while all other parameters were fixed. (b) Rabi splitting of the strong coupling between the WS<sub>2</sub> monolayer and the symmetry-broken QBIC as a function of the  $Q$  factor. Here, sweeping  $C$  swept the  $Q$  factor, while all other parameters were fixed. (c) Rabi splitting of the strong coupling between the perovskite and the symmetry-broken QBIC as a function of the thickness of the nanostructure. (d) Rabi splitting of the strong coupling between the WS<sub>2</sub> monolayer and the symmetry-broken QBIC as a function of the thickness of the nanostructure.

In addition, the operation of double strong coupling in TM-polarization was investigated. As shown in Fig. S3 in the Supplemental Material [68], in the TM polarization, strong coupling occurs only in the perovskite, while WS<sub>2</sub> monolayer remains in the weak coupling. This is because, as previously demonstrated [69], TM-polarized modes are far from resonance with the WS<sub>2</sub> exciton. However, due to the large thickness of the perovskite, the TM-polarized modes can still resonate with its exciton, resulting in the observation of the strong coupling [70].

To understand the strong coupling regime in both materials, we investigate the effect of the  $Q$  factor and the thickness of perovskite thin film on the Rabi splitting. As has been demonstrated before, the  $Q$  factor of the QBIC can be easily tuned by tuning the structure parameters. Therefore, we calculate the Rabi-splitting values at different  $Q$  factor of the symmetry-broken-induced QBIC mode by changing the perovskite NW parameters such as the period of the structure, the center of the slit, and the width of the NW. It is worth mentioning that the  $Q$  factor calculated here is the radiative  $Q$  factor of the lossless perovskite metasurface. Figure 4(a) shows the Rabi splitting of the strong coupling between the symmetry-broken QBIC and the PEPI perovskite as a function of the  $Q$  factor. The results show that the Rabi splitting increases as the  $Q$  factor increases until it saturates at  $\sim 1000$  meV with a maximum Rabi splitting of 380 meV.

In the same way, we investigated the Rabi splitting of the strong coupling between the symmetry-broken-induced QBIC and the WS<sub>2</sub> monolayer. The results are presented in Fig. 4(b).

The saturation of the Rabi splitting was also observed at  $Q \approx 1000$ , reaching its maximum value of  $\sim 42.2$  meV.

Meanwhile, we investigate the effect of varying the NW thickness on the strong coupling of both materials. Figure 4(c) shows the Rabi splitting of the strong coupling regime between the symmetry-broken QBIC and the perovskite exciton as a function of the perovskite NW thickness. It is observed that a higher Rabi splitting of the strong coupling between the PEPI perovskite exciton and the symmetry-broken QBIC is obtained by increasing the thickness of the NWs until it saturates at  $\sim 210$  nm. This is understandable because the electric field is more confined inside the NWs as the thickness of NWs increases. This leads to a larger interaction volume, increasing the coupling strength. On the other hand, the Rabi splitting of the strong coupling between the exciton of the WS<sub>2</sub> monolayer and the symmetry-broken-induced QBIC decreases when the thickness of the NWs increases, as shown in Fig. 4(d). For the case of the WS<sub>2</sub> monolayer, the increased thickness makes the confined electric field distribute over a larger area, reducing the electric field intensity around the WS<sub>2</sub> monolayer and thus weakening the coupling strength. Thus, one must balance thickness so that the coupling strength in both materials can be optimized.

#### D. Dual BIC property of lossless perovskite compound gratings

As discussed earlier, such a grating can excite different leaky modes. Therefore, designing multiple BIC modes simultaneously in a single structure is possible. Here, we choose TE<sub>21</sub> and TE<sub>31</sub> modes to excite two QBIC modes in one structure as an example. Figure 5(a) shows the 2D schematic drawing of the nanostructure supporting double QBIC resonances. The structure consists of a continuous PEPI perovskite film with a height ( $H$ ) of 60 nm underneath a PEPI perovskite NW array with an off-centered slit. Here, we set  $T$ ,  $W$ ,  $G$ , and  $C$  to be 110, 240, 70, and 5 nm, respectively. Figure 5(b) shows the electric field distribution of both symmetry-broken QBIC modes based on the TE<sub>21</sub> and TE<sub>31</sub> modes, respectively. It is evident that eigenfields of both modes are well confined inside the structure, greatly boosting the light-matter interaction. The  $Q$  factors of both symmetry-broken QBIC modes as a function of the period are shown in Fig. 5(c). It is interesting to note that the  $Q$  factors of the TE<sub>21</sub> and TE<sub>31</sub> modes show opposite trends with respect to the period of the structure. In other words, by increasing the structure period, the  $Q$  factor of TE<sub>21</sub> decreases, while the  $Q$  factor of TE<sub>31</sub> increases. This was also confirmed from the reflection mapping data of both symmetry-broken QBIC resonances, as shown in Fig. 5(d). By carefully tuning the structure parameters, the positions of both QBIC resonances can be adjusted to intersect the exciton resonances of the PEPI perovskite and the WS<sub>2</sub> monolayer.

Alternatively, the strong coupling of both QBIC modes could also be realized by fixing the structure parameters and sweeping the angle of incidence. Toward this end, we demonstrate the double strong coupling regime between two QBIC resonances and both excitons of the PEPI perovskite and the WS<sub>2</sub> monolayer by sweeping the angle of incidence. The structure parameters such as  $P$ ,  $T$ ,  $W$ ,  $G$ , and  $C$  are set to 270, 110, 240, 70, and 5 nm, respectively. Figure 5(e) shows

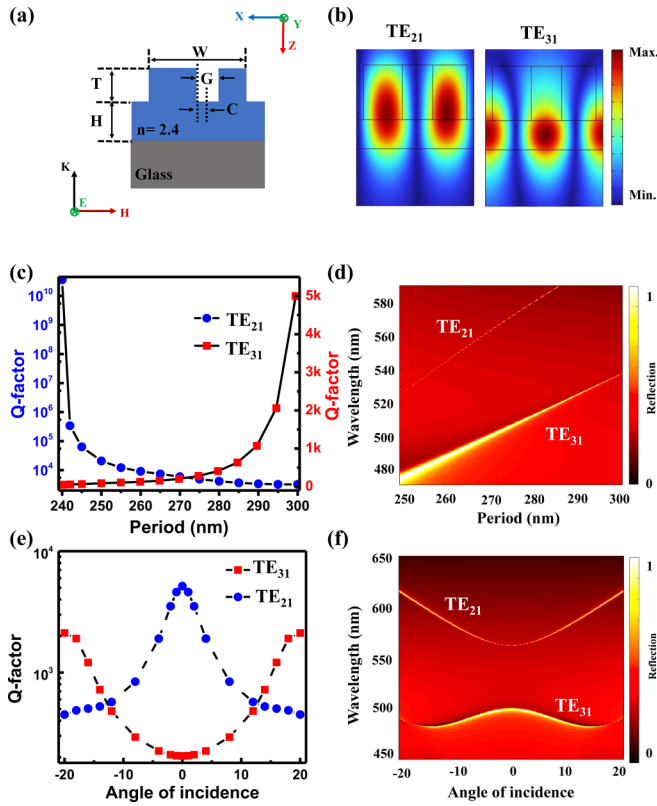


FIG. 5. Double strong coupling based on dual bound-state-in-the-continuum (BIC) mode. (a) Two-dimensional (2D) schematic drawing of the symmetry-broken nanostructure supporting double quasibound-state-in-the-continuum (QBIC) resonances based on PEPI nanowires and a continuous film underneath. (b) The electric field distribution of the  $TE_{21}$  and  $TE_{31}$  modes that supports QBICs. (c) The  $Q$  factor as a function of the period of the symmetry-broken nanostructure supporting dual BIC modes. (d) The mapping data of the reflection spectrum as a function of the period of the structure of the symmetry-broken nanostructure supporting double QBIC resonances. Here, the reflection spectra were obtained by considering both perovskite and glass as lossless materials with refractive indices set to 2.4 and 1.46, respectively. (e) The  $Q$  factor as a function of the angle of incidence on the symmetry-broken nanostructure supporting dual BIC modes. (f) The mapping data of the reflection spectrum as a function of the angle of incidence of the symmetry-broken nanostructure supporting double QBIC resonances. Here, the reflection spectra were obtained by considering both perovskite and glass as lossless materials with refractive indices set to 2.4 and 1.46, respectively.

the calculated  $Q$  factor of the symmetry-broken double QBIC resonances as a function of the angle of incidence while fixing the structure parameters. The  $Q$ -factor calculations show that both resonances have finite  $Q$  factors due to the introduced off-center silt.

Furthermore, the reflection spectrum of both symmetry-broken-induced QBIC modes based on  $TE_{21}$  and  $TE_{31}$  modes is also simulated as a function of incident angle. The mapping data of the reflection spectrum are presented in Fig. 5(f). It is also worth mentioning that the structural parameters were carefully tuned so that each QBIC resonance intersects with one of the exciton resonances. Therefore, here, the QBIC-based  $TE_{31}$  modes are designed to be coupled to the PEPI

perovskite exciton, while the QBIC-based  $TE_{21}$  mode is intended to be coupled to the  $WS_2$  monolayer exciton.

### E. Double strong coupling induced by dual BIC mode

Lastly, after incorporating the  $WS_2$  monolayer in the structure by placing it inside the continuous film of the PEPI perovskite and considering the real and imaginary parts of the refractive indices of both materials, as shown in the schematic drawing in Fig. 6(a), we achieve the strong coupling regime in both materials simultaneously. The  $WS_2$  monolayer is placed at the maxima of the  $TE_{21}$  electric field distribution, which is 5 nm below the perovskite NWs, as shown in Fig. 6(b). Here, the electric field is along the  $Y$  axis, and the structure parameters such as  $H$ ,  $T$ ,  $W$ ,  $G$ , and  $C$  are set to 60, 110, 240, 70, and 5 nm, respectively. Figure 6(b) shows the mapping data of the absorption spectra mapping as a function of the period of the structure. The anticrossing behavior of the  $TE_{31}$  symmetry-broken QBIC and PEPI perovskite exciton is observed at a period of  $\sim 281$  nm. At the same time, the anticrossing behavior of the  $TE_{21}$  symmetry-broken QBIC and  $WS_2$  monolayer exciton occurs at a period of  $\sim 284$  nm. We also fitted the dispersion relationship of the formed polaritons of both strong couplings using Eq. (3). The dispersion relationship of the UPs and LPs of both strong couplings as a function of the period of the structure is shown in Fig. 6(c). The fitting data match well with the mapping data of the absorption spectrum of both strong coupling regimes. A Rabi splitting of  $\sim 348.75$  meV was calculated between the UP and LP of the strong coupling between the  $TE_{31}$ -based QBIC and perovskite exciton, while a Rabi splitting of  $\sim 37.86$  meV was obtained between UP and LP of the strong coupling between the  $TE_{21}$ -based QBIC and  $WS_2$  monolayer exciton. The coupling strength between the QBIC modes and both excitons of perovskite and  $WS_2$  monolayers are calculated using Eq. (4) and found to be 174.38 and 18.93 meV, respectively. The fractions of both strong coupling regimes are presented in Fig. 7.

Furthermore, the double strong coupling regime based on the dual QBIC resonances was also achieved by sweeping the angle of incidence and fixing the structural parameters such as  $P$ ,  $H$ ,  $T$ ,  $W$ ,  $G$ , and  $C$  to 270, 60, 110, 240, 70, and 5 nm, respectively. Figure 6(c) shows the mapping data of the absorption spectrum as a function of incident angle for the dual QBIC resonance based on  $TE_{31}$  and  $TE_{21}$  modes coupled to both excitons of the PEPI perovskite and the  $WS_2$  monolayer, respectively. The absorption spectrum shows the UPs and LPs resulting from the strong coupling of the symmetry-broken  $TE_{31}$ -based QBIC and the PEPI perovskite excitons. The anticrossing behavior happens at a  $2^\circ$  angle, resulting in a Rabi splitting of  $\sim 353.6$  meV. Similarly, the emerging UPs and LPs in the absorption spectrum confirm the strong coupling between the symmetry-broken-induced QBIC based on  $TE_{21}$  mode and the exciton of the  $WS_2$  monolayer. The anticrossing behavior of the  $WS_2$  monolayer happens at an angle of  $13^\circ$ , yielding a Rabi splitting of  $\sim 31.80$  meV. These results were also confirmed by fitting the dispersion relation of the UPs and LPs of both strong coupling regimes using Eq. (3). Figure 6(e) shows the dispersion relationship of the formed polaritons from the double strong coupling regimes as a function of incidence angle. The coupling strength between the QBIC

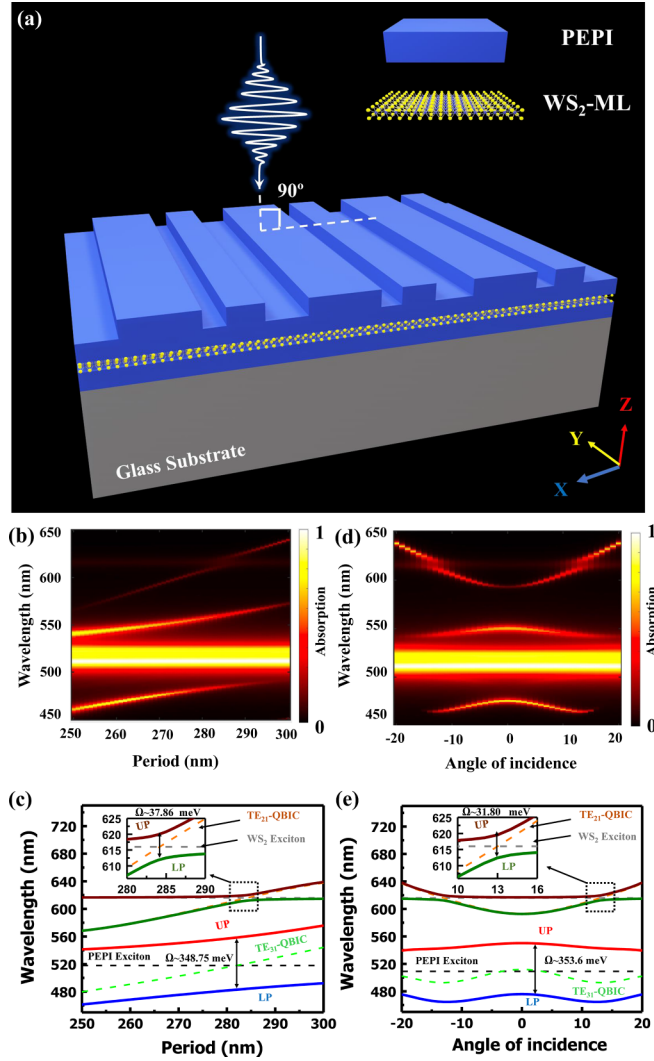


FIG. 6. Observation of double strong coupling regime based on dual bound-state-in-the-continuum (BIC) mode. (a) Three-dimensional (3D) schematic drawing of the symmetry broken nanostructure supporting double QBIC resonances with the  $\text{WS}_2$  monolayer placed inside the continuous film of PEPI perovskite. (b) Mapping data of the absorption spectrum as a function of the period of the structure. Here, the absorption spectra were obtained by considering perovskite as a lossy material with a permittivity calculated using Eq. (1) and glass as a lossless material with a refractive index set to 1.46. (c) The fitting data of the polariton dispersion relationship [upper polariton (UP) in solid red and lower polariton (LP) in solid blue] as a function of the period of the structure of the strong coupling between  $\text{TE}_{31}$ -based QBIC (dashed green) and PEPI-exciton (dashed black), and the fitting data of the polariton dispersion relationship (UP in solid brown and LP in solid olive) as a function of the period of the structure of the strong coupling between  $\text{TE}_{21}$ -based QBIC (dashed orange) and  $\text{WS}_2$  monolayer exciton (dashed gray). The inset shows a magnified cross-section of the anticrossing behavior between the  $\text{WS}_2$  monolayer and  $\text{TE}_{21}$ -based QBIC mode as a function of the period of the structure. (d) Mapping data of the absorption spectrum as a function of the angle of incidence. Here, the absorption spectra were obtained by considering perovskite as a lossy material with a permittivity calculated using Eq. (1) and glass as a lossless material with a refractive index set to 1.46. (e) The fitting data of the polariton dispersion relationship (UP in solid red and LP in solid blue) as a function of the angle of

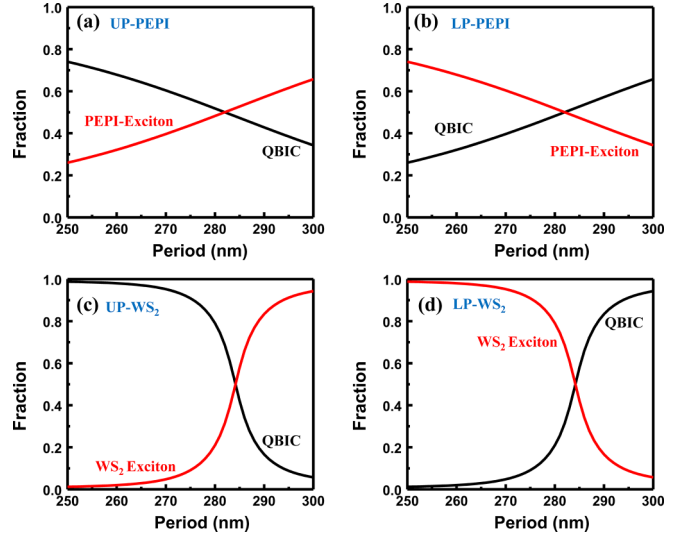


FIG. 7. The fraction of the upper polariton (UP) and lower polariton (LP) branches of the double strong coupling based on double quasibound states in the continuum (QBICs) as a function of the period of the structure. (a) Fractions of the UP branch of the strong coupling between  $\text{TE}_{31}$ -based QBIC in solid black and PEPI-exciton in solid red as a function of the period of the structure. (b) Fractions of the LP branch of the strong coupling between  $\text{TE}_{31}$ -based QBIC in solid black and PEPI-exciton in solid red as a function of the period of the structure. (c) Fractions of the UP branch of the strong coupling between  $\text{TE}_{21}$ -based QBIC in solid black and  $\text{WS}_2$  monolayer exciton in solid red as a function of the period of the structure. (d) Fractions of the LP branch of the strong coupling between  $\text{TE}_{21}$ -based QBIC in solid black and  $\text{WS}_2$  monolayer exciton in solid red as a function of the period of the structure.

modes and both excitons of perovskite and  $\text{WS}_2$  monolayers are calculated using Eq. (4) and found to be 176.84 and 16.30 meV, respectively. The fractions of both strong coupling regimes are presented in Fig. S4 in the Supplemental Material [68]. Finally, it is worth mentioning that such a design enables the observation of double strong coupling regimes by only sweeping the incident angle, greatly simplifying the requirements of the experiment of such a system where only one structure is needed.

### III. CONCLUSIONS

We have demonstrated room-temperature double exciton-polaritons by strongly coupling excitons in perovskite and  $\text{WS}_2$  monolayers to either single QBIC or double QBICs. A one-dimensional all-perovskite dielectric grating was used to design symmetry-protected and symmetry-broken QBIC

← incidence of the strong coupling between  $\text{TE}_{31}$ -based QBIC (dashed green) and PEPI-exciton (dashed black), and the fitting data of the polariton dispersion relationship (UP in solid brown and LP in solid olive) as a function of the angle of incidence of the strong coupling between  $\text{TE}_{21}$ -based QBIC (dashed orange) and  $\text{WS}_2$  monolayer exciton (dashed gray). The inset shows a magnified cross-section of the anticrossing behavior between the  $\text{WS}_2$  monolayer and  $\text{TE}_{21}$ -based QBIC mode as a function of the angle of incidence.



based on the  $TE_{21}$  modes. Using this design technique, we have achieved a Rabi splitting as high as 380 and 42.2 meV in the perovskite and  $WS_2$  monolayers, respectively. Furthermore, the effect of varying the  $Q$  factor and the thickness of the nanostructure on the Rabi splitting were investigated. We also found that the Rabi splitting could be tuned to its maximum value by tuning the  $Q$  factor and thickness of the nanostructure. Both strong couplings in the perovskite and  $WS_2$  monolayers have increased the Rabi splitting by increasing the  $Q$  factor until it saturates at a particular value.

On the other hand, coupling strength in the  $WS_2$  monolayer and perovskite has shown an opposite trend with the thickness

of the nanostructure. Finally, a dual QBIC mode was designed based on the  $TE_{21}$  and  $TE_{31}$  modes and strongly coupled to the perovskite and  $WS_2$  monolayer excitons. This design approach achieved a Rabi splitting as high as  $\sim 353.6$  meV and  $\sim 31.80$  meV in the perovskite and  $WS_2$  monolayers, respectively. Our results open the way for developing polaritonic applications such as dual-wavelength polariton nanolasers.

## ACKNOWLEDGMENTS

This work is supported by an Australian Government Research Training Program (RTP) Scholarship.

- 
- [1] I. A. M. Al-Ani, K. As'Ham, O. Klochan, H. T. Hattori, L. Huang, and A. E. Miroshnichenko, Recent advances on strong light-matter coupling in atomically thin TMDC semiconductor materials, *J. Opt.* **24**, 053001 (2022).
- [2] L. Huang, A. Krasnok, A. Alú, Y. Yu, D. Neshev, and A. E. Miroshnichenko, Enhanced light-matter interaction in two-dimensional transition metal dichalcogenides, *Rep. Prog. Phys.* **85**, 046401 (2022).
- [3] C. Schneider, M. M. Glazov, T. Korn, S. Höfling, and B. Urbaszek, Two-dimensional semiconductors in the regime of strong light-matter coupling, *Nat. Commun.* **9**, 2695 (2018).
- [4] T. Low, A. Chaves, J. D. Caldwell, A. Kumar, N. X. Fang, P. Avouris, T. F. Heinz, F. Guinea, L. Martin-Moreno, and F. Koppens, Polaritons in layered two-dimensional materials, *Nat. Mater.* **16**, 182 (2016).
- [5] F. Hu and Z. Fei, Recent progress on exciton polaritons in layered transition-metal dichalcogenides, *Adv. Opt. Mater.* **8**, 1901003 (2020).
- [6] P. A. D. Gonçalves, N. Stenger, J. D. Cox, N. A. Mortensen, and S. Xiao, Strong light-matter interactions enabled by polaritons in atomically thin materials, *Adv. Opt. Mater.* **8**, 1901473 (2020).
- [7] X. Liu, T. Galfsky, Z. Sun, F. Xia, E. Lin, Y.-H. Lee, S. Kéna-Cohen, and V. M. Menon, Strong light-matter coupling in two-dimensional atomic crystals, *Nat. Photonics* **9**, 30 (2014).
- [8] A. Amo, T. C. H. Liew, C. Adrados, R. Houdré, E. Giacobino, A. V. Kavokin, and A. Bramati, Exciton-polariton spin switches, *Nat. Photonics* **4**, 361 (2010).
- [9] D. G. Lidzey, D. D. C. Bradley, M. S. Skolnick, T. Virgili, S. Walker, and D. M. Whittaker, Strong exciton-photon coupling in an organic semiconductor microcavity, *Nature (London)* **395**, 53 (1998).
- [10] H. Wang, H. Y. Wang, A. Toma, T. A. Yano, Q. D. Chen, H. L. Xu, H. B. Sun, and R. Proietti Zaccaria, Dynamics of strong coupling between CdSe quantum dots and surface plasmon polaritons in subwavelength hole array, *J. Phys. Chem. Lett.* **7**, 4648 (2016).
- [11] M. Wurdack, N. Lundt, M. Klaas, V. Baumann, A. V. Kavokin, S. Höfling, and C. Schneider, Observation of hybrid Tamm-plasmon exciton-polaritons with GaAs quantum wells and a  $MoSe_2$  monolayer, *Nat. Commun.* **8**, 259 (2017).
- [12] K. As'ham, I. Al-Ani, W. Lei, H. T. Hattori, L. Huang, and A. Miroshnichenko, Mie Exciton-Polariton in a Perovskite Meta-surface, *Phys. Rev. Appl.* **18**, 014079 (2022).
- [13] V. Agranovich, H. Benisty, and C. Weisbuch, Organic and inorganic quantum wells in a microcavity: Frenkel-Wannier-Mott excitons hybridization and energy transformation, *Solid State Commun.* **102**, 631 (1997).
- [14] J. Wainstain, C. Delalande, D. Gendt, M. Voos, J. Bloch, V. Thierry-Mieg, and R. Planel, Dynamics of polaritons in a semiconductor multiple-quantum-well microcavity, *Phys. Rev. B* **58**, 7269 (1998).
- [15] D. G. Lidzey, D. D. C. Bradley, A. Armitage, S. Walker, and M. S. Skolnick, Photon-mediated hybridization of Frenkel excitons in organic semiconductor microcavities, *Science* **288**, 1620 (2000).
- [16] D. M. Coles, N. Somaschi, P. Michetti, C. Clark, P. G. Lagoudakis, P. G. Savvidis, and D. G. Lidzey, Polariton-mediated energy transfer between organic dyes in a strongly coupled optical microcavity, *Nat. Mater.* **13**, 712 (2014).
- [17] J. Wenus, R. Parashkov, S. Ceccarelli, A. Brehier, J. S. Lauret, M. S. Skolnick, E. Deleporte, and D. G. Lidzey, Hybrid organic-inorganic exciton-polaritons in a strongly coupled microcavity, *Phys. Rev. B* **74**, 235212 (2006).
- [18] G. Lanty, S. Zhang, J. S. Lauret, E. Deleporte, P. Audebert, S. Bouchoule, X. Lafosse, J. Zuñiga-Pérez, F. Semond, D. Lagarde *et al.*, Hybrid cavity polaritons in a ZnO-perovskite microcavity, *Phys. Rev. B* **84**, 195449 (2011).
- [19] M. Wang, M. Hertzog, and K. Börjesson, Polariton-assisted excitation energy channeling in organic heterojunctions, *Nat. Commun.* **12**, 1874 (2021).
- [20] K. Georgiou, R. Jayaprakash, A. Othonos, and D. G. Lidzey, Ultralong-range polariton-assisted energy transfer in organic microcavities, *Angew. Chem.* **133**, 16797 (2021).
- [21] K. Zhang, W. B. Shi, D. Wang, Y. Xu, R. W. Peng, R. H. Fan, Q. J. Wang, and M. Wang, Couple molecular excitons to surface plasmon polaritons in an organic-dye-doped nanostructured cavity, *Appl. Phys. Lett.* **108**, 193111 (2016).
- [22] M. Balasubrahmaniam, D. Kar, P. Sen, P. B. Bisht, and S. Kasiviswanathan, Observation of subwavelength localization of cavity plasmons induced by ultra-strong exciton coupling, *Appl. Phys. Lett.* **110**, 171101 (2017).
- [23] D. Melnikau, A. A. Goyadinov, A. Sánchez-Iglesias, M. Grzelczak, I. R. Nabiev, L. M. Liz-Marzán, and Y. P. Rakovich, Double Rabi splitting in a strongly coupled system of core-shell Au@Ag nanorods and J-aggregates of multiple fluorophores, *J. Phys. Chem. Lett.* **10**, 6137 (2019).
- [24] H. Yang, J. Yao, X. W. Wu, D. J. Wu, and X. J. Liu, Strong plasmon-exciton-plasmon multimode couplings

- in three-layered Ag-J-aggregates-Ag nanostructures, *J. Phys. Chem. C* **121**, 25455 (2017).
- [25] S. Balci and C. Kocabas, Ultra hybrid plasmonics: Strong coupling of plexcitons with plasmon polaritons, *Opt. Lett.* **40**, 3424 (2015).
- [26] B. Li, S. Zu, Z. Zhang, L. Zheng, Q. Jiang, B. Du, Y. Luo, Y. Gong, Y. Zhang, F. Lin *et al.*, Large Rabi splitting obtained in Ag-WS<sub>2</sub> strong-coupling heterostructure with optical microcavity at room temperature, *Opto-Electron. Adv.* **2**, 190008 (2019).
- [27] J. Cuadra, D. G. Baranov, M. Wersäll, R. Verre, T. J. Antosiewicz, and T. Shegai, Observation of tunable charged exciton polaritons in hybrid monolayer WS<sub>2</sub>-plasmonic nanoantenna system, *Nano Lett.* **18**, 1777 (2018).
- [28] H. Li, Q. Ai, Y. Li, X. Zhai, T. Liu, Y. Ren, and T. Gao, Localization of anisotropic exciton polariton condensates in perovskite microcavities, *Appl. Phys. Lett.* **120**, 11104 (2022).
- [29] R. Su, S. Ghosh, J. Wang, S. Liu, C. Diederichs, T. C. H. Liew, and Q. Xiong, Observation of exciton polariton condensation in a perovskite lattice at room temperature, *Nat. Phys.* **16**, 301 (2020).
- [30] L. Polimeno, A. Fieramosca, G. Lerario, M. Cinquino, M. De Giorgi, D. Ballardini, F. Todisco, L. Dominici, V. Ardizzone, M. Pugliese *et al.*, Observation of two thresholds leading to polariton condensation in 2D hybrid perovskites, *Adv. Opt. Mater.* **8**, 2000176 (2020).
- [31] M. E. Kleemann, R. Chikkaraddy, E. M. Alexeev, D. Kos, C. Carnegie, W. Deacon, A. C. de Pury, C. Große, B. de Nijs, J. Mertens *et al.*, Strong-coupling of WSe<sub>2</sub> in ultra-compact plasmonic nanocavities at room temperature, *Nat. Commun.* **8**, 1296 (2017).
- [32] W. Liu, B. Lee, C. H. Naylor, H. S. Ee, J. Park, A. T. C. Johnson, and R. Agarwal, Strong exciton-plasmon coupling in MoS<sub>2</sub> coupled with plasmonic lattice, *Nano Lett.* **16**, 1262 (2016).
- [33] J. Lawless, C. Hrelescu, C. Elliott, L. Peters, N. McEvoy, and A. L. Bradley, Influence of gold nano-bipyramid dimensions on strong coupling with excitons of monolayer MoS<sub>2</sub>, *ACS Appl. Mater. Interfaces* **12**, 46406 (2020).
- [34] X. Yan and H. Wei, Strong plasmon-exciton coupling between lithographically defined single metal nanoparticles and monolayer WSe<sub>2</sub>, *Nanoscale* **12**, 9708 (2020).
- [35] J. Sun, Y. Li, H. Hu, W. Chen, D. Zheng, S. Zhang, and H. Xu, Strong plasmon-exciton coupling in transition metal dichalcogenides and plasmonic nanostructures, *Nanoscale* **13**, 4408 (2021).
- [36] L. Liu, L. Y. M. Tobing, X. Yu, J. Tong, B. Qiang, A. I. Fernández-Domínguez, F. J. Garcia-Vidal, D. H. Zhang, Q. J. Wang, and Y. Luo, Strong plasmon-exciton interactions on nanoantenna array-monolayer WS<sub>2</sub> hybrid system, *Adv. Opt. Mater.* **8**, 1901002 (2020).
- [37] F. Deng, H. Liu, L. Xu, S. Lan, and A. E. Miroshnichenko, Strong exciton-plasmon coupling in a WS<sub>2</sub> monolayer on Au film hybrid structures mediated by liquid Ga nanoparticles, *Laser Photon Rev.* **14**, 1900420 (2020).
- [38] M. Stührenberg, B. Munkhbat, D. G. Baranov, J. Cuadra, A. B. Yankovich, T. J. Antosiewicz, E. Olsson, and T. Shegai, Strong light-matter coupling between plasmons in individual gold bipyramids and excitons in mono- and multilayer WSe<sub>2</sub>, *Nano Lett.* **18**, 5938 (2018).
- [39] D. Zheng, S. Zhang, Q. Deng, M. Kang, P. Nordlander, and H. Xu, Manipulating coherent plasmon-exciton interaction in a single silver nanorod on monolayer WSe<sub>2</sub>, *Nano Lett.* **17**, 3809 (2017).
- [40] X. Han, K. Wang, X. Xing, M. Wang, and P. Lu, Rabi splitting in a plasmonic nanocavity coupled to a WS<sub>2</sub> monolayer at room temperature, *ACS Photonics* **5**, 3970 (2018).
- [41] I. A. M. Al-Ani, K. As'Ham, L. Huang, A. E. Miroshnichenko, and H. T. Hattori, Enhanced strong coupling of TMDC monolayers by bound state in the continuum, *Laser Photon Rev.* **15**, 2100240 (2021).
- [42] N. Lundt, S. Klembt, E. Cherotchenko, S. Betzold, O. Iff, A. V. Nalitov, M. Klaas, C. P. Dietrich, A. V. Kavokin, S. Höfling *et al.*, Room-temperature Tamm-plasmon exciton-polaritons with a WSe<sub>2</sub> monolayer, *Nat. Commun.* **7**, 13328 (2016).
- [43] L. C. Flatten, Z. He, D. M. Coles, A. A. P. Trichet, A. W. Powell, R. A. Taylor, J. H. Warner, and J. M. Smith, Room-temperature exciton-polaritons with two-dimensional WS<sub>2</sub>, *Sci. Rep.* **6**, 33134 (2016).
- [44] N. Lundt, A. Maryński, E. Cherotchenko, A. Pant, X. Fan, S. Tongay, G. Şek, A. V. Kavokin, S. Höfling, and C. Schneider, Monolayered MoSe<sub>2</sub>: A candidate for room temperature polaritonics, *2D Mater.* **4**, 015006 (2016).
- [45] L. Lackner, M. Dusel, O. A. Egorov, B. Han, H. Knopf, F. Eilenberger, S. Schröder, K. Watanabe, T. Taniguchi, S. Tongay *et al.*, Tunable exciton-polaritons emerging from WS<sub>2</sub> monolayer excitons in a photonic lattice at room temperature, *Nat. Commun.* **12**, 4933 (2021).
- [46] M. Król, K. Rechcińska, K. Nogajewski, M. Grzeszczyk, K. Łempicka, R. Mirek, S. Piotrowska, K. Watanabe, T. Taniguchi, M. R. Molas *et al.*, Exciton-polaritons in multilayer WSe<sub>2</sub> in a planar microcavity, *2D Mater.* **7**, 015006 (2019).
- [47] K. As'Ham, I. Al-Ani, L. Huang, A. E. Miroshnichenko, and H. T. Hattori, Boosting strong coupling in a hybrid WSe<sub>2</sub> monolayer-anapole-plasmon system, *ACS Photonics* **8**, 489 (2021).
- [48] S. Wang, S. Li, T. Chervy, A. Shalabney, S. Azzini, E. Orgiu, J. A. Hutchison, C. Genet, P. Samorì, and T. W. Ebbesen, Coherent coupling of WS<sub>2</sub> monolayers with metallic photonic nanostructures at room temperature, *Nano Lett.* **16**, 4368 (2016).
- [49] A. I. Kuznetsov, A. E. Miroshnichenko, M. L. Brongersma, Y. S. Kivshar, and B. Luk'yanchuk, Optically resonant dielectric nanostructures, *Science* **354**, eaag2472 (2016).
- [50] Y. He, G. Guo, T. Feng, Y. Xu, and A. E. Miroshnichenko, Toroidal dipole bound states in the continuum, *Phys. Rev. B* **98**, 161112(R) (2018).
- [51] K. L. Koshelev, S. K. Sychev, Z. F. Sadrieva, A. A. Bogdanov, and I. V. Iorsh, Strong coupling between excitons in transition metal dichalcogenides and optical bound states in the continuum, *Phys. Rev. B* **98**, 161113(R) (2018).
- [52] C. W. Hsu, B. Zhen, A. D. Stone, J. D. Joannopoulos, and M. Soljacic, Bound states in the continuum, *Nat. Rev. Mater.* **1**, 16048 (2016).
- [53] S. I. Azzam and A. V. Kildishev, Photonic bound states in the continuum: From basics to applications, *Adv. Opt. Mater.* **9**, 2001469 (2021).
- [54] L. Huang, Y. K. Chiang, S. Huang, C. Shen, F. Deng, Y. Cheng, B. Jia, Y. Li, D. A. Powell, and A. E. Miroshnichenko, Sound trapping in an open resonator, *Nat. Commun.* **12**, 4819 (2021).

- [55] M. Qin, S. Xiao, W. Liu, M. Ouyang, T. Yu, T. Wang, and Q. Liao, Strong coupling between excitons and magnetic dipole quasi-bound states in the continuum in WS<sub>2</sub>-TiO<sub>2</sub> hybrid metasurfaces, *Opt. Express* **29**, 18026 (2021).
- [56] S. Cao, H. Dong, J. He, E. Forsberg, Y. Jin, and S. He, Normal-incidence-excited strong coupling between excitons and symmetry-protected quasi-bound states in the continuum in silicon nitride-WS<sub>2</sub> heterostructures at room temperature, *J. Phys. Chem. Lett.* **11**, 4631 (2020).
- [57] V. Kravtsov, E. Khestanova, F. A. Benimetskiy, T. Ivanova, A. K. Samusev, I. S. Sinev, D. Pidgayko, A. M. Mozharov, I. S. Mukhin, M. S. Lozhkin *et al.*, Nonlinear polaritons in a monolayer semiconductor coupled to optical bound states in the continuum, *Light Sci. Appl.* **9**, 56 (2020).
- [58] L. Lu, Q. Le-Van, L. Ferrier, E. Drouard, C. Seassal, H. S. Nguyen, and H. S. Nguyen, Engineering a light-matter strong coupling regime in perovskite-based plasmonic metasurface: Quasi-bound state in the continuum and exceptional points, *Photonics Res.* **8**, A91 (2020).
- [59] P. Xie, Z. Liang, T. Jia, D. Li, Y. Chen, P. Chang, H. Zhang, and W. Wang, Strong coupling between excitons in a two-dimensional atomic crystal and quasibound states in the continuum in a two-dimensional all-dielectric asymmetric metasurface, *Phys. Rev. B* **104**, 125446 (2021).
- [60] M. Qin, J. Duan, S. Xiao, W. Liu, T. Yu, T. Wang, and Q. Liao, Manipulating strong coupling between exciton and quasibound states in the continuum resonance, *Phys. Rev. B* **105**, 195425 (2022).
- [61] I. A. M. Al-Ani, K. As'Ham, L. Huang, A. E. Miroschnichenko, W. Lei, and H. T. Hattori, Strong coupling of exciton and high- $Q$  mode in all-perovskite metasurfaces, *Adv. Opt. Mater.* **10**, 2101120 (2022).
- [62] S. Zhang, P. Audebert, Y. Wei, A. Al Choueiry, G. Lanty, A. Bréhier, L. Galmiche, G. Clavier, C. Boissière, J.-S. Lauret *et al.*, Preparations and characterizations of luminescent two dimensional organic-inorganic perovskite semiconductors, *Materials* **3**, 3385 (2010).
- [63] N. H. M. Dang, D. Gerace, E. Drouard, G. Trippé-Allard, F. Lédéé, R. Mazurczyk, E. Deleporte, C. Seassal, and H. S. Nguyen, Tailoring dispersion of room-temperature exciton-polaritons with perovskite-based subwavelength metasurfaces, *Nano Lett.* **20**, 2113 (2020).
- [64] L. Huang, Y. Yu, and L. Cao, General modal properties of optical resonances in subwavelength nonspherical dielectric structures, *Nano Lett.* **13**, 3559 (2013).
- [65] L. Huang, G. Li, A. Gurarslan, Y. Yu, R. Kirste, W. Guo, J. Zhao, R. Collazo, Z. Sitar, G. N. Parsons *et al.*, Atomically thin MoS<sub>2</sub> narrowband and broadband light superabsorbers, *ACS Nano* **10**, 7493 (2016).
- [66] R. Gogna, L. Zhang, Z. Wang, H. Deng, and H. Deng, Photonic crystals for controlling strong coupling in van der Waals materials, *Opt. Express* **27**, 22700 (2019).
- [67] Y. Li, A. Chernikov, X. Zhang, A. Rigosi, H. M. Hill, A. M. Van Der Zande, D. A. Chenet, E. M. Shih, J. Hone, and T. F. Heinz, Measurement of the optical dielectric function of monolayer transition-metal dichalcogenides: MoS<sub>2</sub>, MoSe<sub>2</sub>, WS<sub>2</sub>, and WSe<sub>2</sub>, *Phys. Rev. B* **90**, 205422 (2014).
- [68] See Supplemental Material at <http://link.aps.org/supplemental/10.1103/PhysRevB.108.045420> for the permittivity of the monolayer, the fraction of the polariton branches of the double strong coupling, and the double strong coupling investigation for TM polarization.
- [69] L. Zhang, R. Gogna, W. Burg, E. Tutuc, and H. Deng, Photonic-crystal exciton-polaritons in monolayer semiconductors, *Nat. Commun.* **9**, 713 (2018).
- [70] K. Zhang, R.-W. Peng, M. Wang, T.-Y. Chen, Q.-J. Wang, W.-B. Shi, C.-Y. Li, and R.-H. Fan, Polarization-dependent strong coupling between surface plasmon polaritons and excitons in an organic-dye-doped nanostructure, *Opt. Lett.* **42**, 2834 (2017).